J. Fluid Mech. (2006), *vol.* 556, *pp.* 167–188. © 2006 Cambridge University Press
doi:10.1017/S0022112006009384 Printed in the United Kingdom

Shear-driven and channel flow of a liquid film over a corrugated or indented wall

By H. LUO AND C. POZRIKIDIS†

Department of Mechanical and Aerospace Engineering, University of California, San Diego, La Jolla, CA 92093-0411, USA

(Received 24 July 2005 and in revised form 9 November 2005)

The shape of the interface between two superimposed layers in a two-dimensional channel confined between a planar and a corrugated or indented wall is investigated in the limit of Stokes flow. A perturbation analysis for walls with small-amplitude sinusoidal corrugations reveals that an insoluble surfactant amplifies the deformation of the interface and causes a negative drift in the phase shift under most conditions. The effect is most significant at moderate capillary numbers and for corrugations whose wavelength is large compared to the thickness of the adjacent layer lining the wavy wall. The precise effect of the surfactant depends on the ratio of the fluid viscosities, proximity of the interface to the planar wall, capillary number, and wavelength of the corrugations. When the interface is near the plane wall, introducing surfactant reduces the interfacial amplitude and causes a positive phase shift with respect to the wavy wall. As the interface further approaches the plane wall, the interfacial wave tends to become in phase with the wavy wall, reflecting its unshifted topography. In the second part of this study, a boundary integral method is implemented to compute Stokes flow over a wall with an arbitrary periodic profile, and results are presented for sinusoidal walls and planar walls containing a periodic sequence of square and circular depressions or projections. The numerical results reveal that the linear perturbation theory overestimates the deformation of the interface over a wavy wall, and illustrate the nature of shear-driven film flow over a planar wall with indented topography.

1. Introduction

Sheared liquid films and layers in channels and down inclined walls are encountered in a wide variety of natural and engineering applications. Examples can be found in coating and extrusion processes, two-phase flow through porous media and microdevices, hydrodynamic cleaning of rough surfaces and fabricated micro-channels, and core–annular flow through straight and corrugated tubes occurring in lubricated pipelining. The gravity- and inertia-driven flow of single and multiple liquid films over planar, wavy and indented walls has been studied extensively by analytical, experimental and computational methods under a broad range of flow conditions (e.g. Kalliadasis, Bielarz & Homsy 2000; Mazouchi & Homsy 2001; Pozrikidis 2003, 2004; Blyth & Pozrikidis 2004*b*). The pressure- and gravity-driven unidirectional channel flow of two and multiple layers has also been considered in detail with emphasis on interfacial stability due to viscosity stratification and presence of a surfactant (e.g. Pozrikidis 2004). In contrast, the effect of wall corrugations or indented topography

† Author to whom correspondence should be addressed: cpozrikidis@ucsd.edu.

on the structure of an effectively semi-infinite shear-driven flow or confined channel flow has been considered on only few occasions.

Dassori, Deiber & Cassano (1984) studied the steady flow of three layers in a vertical channel with symmetric sinusoidal walls and equal wall-layer thicknesses, subject to the restriction that the amplitude of corrugations, a_W, is small compared to the mean thickness of the middle fluid, h, so that $\epsilon \equiv a_W/h \ll 1$. The Reynolds number was assumed to be of the order of the expansion parameter ϵ. Their analysis revealed that the interface develops a wavy profile with a relative phase shift with respect to the sinusoidal walls. Their results illustrated the dependence of the interfacial amplitude and phase shift on the wavelength of the corrugations and on the various flow parameters.

Other authors have considered the structure and stability of axisymmetric core–annular flow through tubes with sinusoidal corrugations. Kouris & Tsamopoulos (2000, 2001) investigated core–annular flow though a tube with long wavy corrugations and studied the effect of the undulations on the stability of the base flow for small wavenumbers based on the lubrication approximation. Because the base flow is non-unidirectional, the superharmonic Fourier modes of the perturbation do not decouple, and a two-dimensional eigenvalue problem must be solved by numerical methods. Wei & Rumschitzki (2002*a*, *b*) performed a similar linear and weakly nonlinear stability analysis in the limit where the thickness of the annular film is small compared to the mean core radius and the amplitude of the corrugations is small compared to the film thickness. Under these conditions, the dynamics of both the base and unsteady perturbation flow are determined by the flow in the annular film alone. The mathematical formulation culminates in a one-dimensional partial differential equation with non-constant coefficients whose eigenfunction can be expressed as the product of a monochromatic disturbance and an infinite series containing harmonics of the wall wave. Kouris & Tsamopoulos (2000, 2001) and Wei & Rumschitzki (2002*a*, *b*) both found that wall corrugations render the flow more prone to instability. A study of the structure and stability of the core–annular flow for large-amplitude corrugations and for perturbations of arbitrary wavelength is not available at present.

In this paper, we investigate the structure of the steady two-layer flow in a two-dimensional channel confined by a planar upper wall and an uneven lower wall in the limit of vanishing Reynolds number, accounting for the presence of an insoluble surfactant. The main objective is to describe the shape of the interface and assess the effect of the surfactant in light of the recent discovery that the Marangoni traction due to variations in the surfactant concentration may amplify the deformation of the free surface of a liquid film down an inclined wall (Pozrikidis 2003; Blyth & Pozrikidis 2004*b*). In § 2, we present the problem statement and outline the governing equations. In § 3, we develop a perturbation analysis for small-amplitude sinusoidal corrugations and carry out an extensive parametric investigation. In § 4, we develop a boundary integral method for unsteady flow over a wall with an arbitrary periodic profile, and present numerical solutions for walls with sinusoidal corrugations and planar walls containing circular and rectangular indentations. We conclude in § 5 by summarizing the results and presenting a tentative discussion of the effect of the corrugations on the stability of the base flow described in the preceding sections.

2. Problem statement

We consider the steady, two-dimensional flow of two superimposed viscous layers in a horizontal or inclined channel confined by a planar upper wall and a periodic lower wall, as illustrated in figure 1(*a*). The lower fluid is labelled as fluid 1, and the

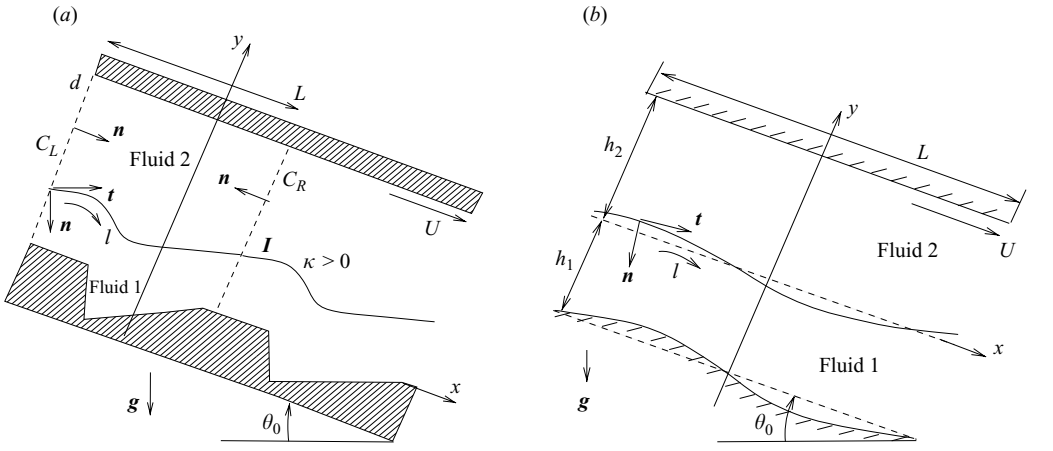

FIGURE 1. Schematic illustration of two-layer flow in a channel with a planar upper wall and (*a*) an uneven lower wall with arbitrary geometry, or (*b*) a sinusoidal lower wall.

upper fluid as fluid 2. The motion may be driven by the translation of the upper wall parallel to itself with velocity U, an imposed streamwise pressure gradient, or gravity. The Reynolds number of the flow based on the channel width is assumed to be so small that the motion of both fluids is governed by the linear equations Stokes flow, including the Stokes equation and the continuity equation,

$$-\nabla p + \mu_j \nabla^2 \boldsymbol{u} + \rho_j \boldsymbol{g} = \boldsymbol{0}, \qquad \nabla \cdot \boldsymbol{u} = 0, \tag{2.1}$$

where $j = 1, 2$, respectively, for the lower and upper fluid, μ_j and ρ_j are the liquid viscosities and densities, $\boldsymbol{u} = (u,\ v)$ is the velocity, p is the pressure, and $\boldsymbol{g}$ is the acceleration due to gravity.

The velocity is required to satisfy the no-slip and no-penetration conditions at the upper and lower wall. The velocity is continuous at the interface, but the hydrodynamic traction undergoes a discontinuity given by

$$\Delta \boldsymbol{f} \equiv \left(\boldsymbol{\sigma}^{(1)} - \boldsymbol{\sigma}^{(2)}\right) \cdot \boldsymbol{n} = -\gamma\kappa\, \boldsymbol{n} - \frac{\partial \gamma}{\partial l}\, \boldsymbol{t}, \tag{2.2}$$

where $\boldsymbol{\sigma}^{(j)}$ is the Newtonian stress tensor on the side of the jth fluid, γ is a position-dependent surface tension, $\boldsymbol{n}$ is the unit normal vector pointing into the lower fluid, $\boldsymbol{t}$ is the unit tangential vector pointing in the direction of increasing arclength l, and $\kappa = \boldsymbol{n} \cdot \mathrm{d}\boldsymbol{t}/\mathrm{d}l$ is the curvature of the interface in the (x, y)-plane, reckoned to be positive when the interface is downward parabolic, as illustrated in figure 1(*a*).

The surface tension, γ, depends on the surfactant concentration of an insoluble surfactant, Γ, whose evolution is governed by the convection–diffusion equation

$$\frac{\mathrm{d}\Gamma}{\mathrm{d}t} + \frac{\partial (u_t \Gamma)}{\partial l} = -\Gamma \kappa u_n + D_s \frac{\partial^2 \Gamma}{\partial l^2}, \tag{2.3}$$

where $u_t = \boldsymbol{u} \cdot \boldsymbol{t}$ is the tangential velocity, $u_n = -\boldsymbol{u} \cdot \boldsymbol{n}$ is the normal velocity, and D_s is the surfactant diffusivity (e.g. Li & Pozrikidis 1997; Pozrikidis 2001). The derivative $\mathrm{d}/\mathrm{d}t$ on the left-hand side of (2.3) expresses the rate of change of a variable following the motion of interfacial marker points moving with the component of the fluid velocity normal to the interface. In the case of steady flow, the first terms on the left- and right-hand sides of (2.3) are zero, and the two surviving terms express a balance between interfacial convection and diffusion.

When the surfactant concentration is well below the saturation level, a linear relationship may be assumed between the surface tension and the surfactant concentration according to Gibbs' law, $\gamma_c - \gamma = \Gamma E$, where E is the surface elasticity and γ_c is the surface tension of a clean interface which is devoid of surfactants (e.g. Adamson 1990; Pozrikidis 2004). In terms of the dimensionless physiochemical parameter $\beta = \Gamma_0 E/\gamma_c$, the linear equation of state reads

$$\gamma = \frac{\gamma_0}{1-\beta}\left(1 - \beta\frac{\Gamma}{\Gamma_0}\right), \tag{2.4}$$

where Γ_0 is a reference concentration corresponding to the surface tension $\gamma_0 = \gamma_c(1-\beta)$. The significance of the surfactant is expressed by the dimensionless Marangoni number,

$$Ma \equiv \frac{E\Gamma_0}{\gamma_0} = \frac{\beta}{1-\beta}. \tag{2.5}$$

Our objective is to study the effect of the lower wall geometry, physical properties of the fluids, and Marangoni tension due to the surfactant on the structure of the flow and shape of the interface at steady state.

3. Flow over a wall with small-amplitude sinusoidal corrugations

Progress by analytical methods can be made by considering flow over a wall with small-amplitude sinusoidal corrugations, and performing a perturbation analysis around the planar configuration. The perturbation velocity components, u and v, streamfunction, ψ, and pressure, p, are expanded in perturbation series,

$$(u_j,\ v_j,\ \psi_j,\ p_j) = \left(u_j^{(0)},\ v_j^{(0)},\ \psi_j^{(0)},\ p_j^{(0)}\right) + \epsilon\left(u_j^{(1)},\ v_j^{(1)},\ \psi_j^{(1)},\ p_j^{(1)}\right) + \ldots, \tag{3.1}$$

for $j = 1, 2$. The zeroth-order solution corresponds to unidirectional two-layer channel flow with lower-layer thickness h_1, upper-layer thickness h_2, and channel width $d = h_1 + h_2 \equiv 2h$. To simplify the calculations, we temporarily shift the origin of the y-axis to the location of the unperturbed interface, as illustrated in figure 1(b). The zeroth-order velocity field is given by

$$u_j^{(0)} = -\frac{\chi + \rho_j g_x}{2\mu_j}\, y^2 + \xi_j\, y + u_I, \qquad v_j^{(0)} = 0, \tag{3.2}$$

for $j = 1, 2$, where χ is the negative of the axial pressure gradient, $g_x = g\sin\theta_0$ is the x-component of the acceleration due to gravity, $g = |\boldsymbol{g}|$ is the magnitude of the acceleration due to gravity, u_I is the interfacial velocity given by

$$u_I = \frac{\lambda}{\lambda + r}\, U + \frac{h^2}{\mu_1}\left(\chi + \rho_1 g_x \frac{1+\delta r}{1+r}\right)\frac{2r}{(1+r)(\lambda+r)}, \tag{3.3}$$

U is the velocity of the upper wall, $\lambda = \mu_2/\mu_1$ is the viscosity ratio, $\delta = \rho_2/\rho_1$ is the density ratio, $r = h_2/h_1$ is the layer thickness ratio, and $h = d/2$ is half the channel width. The coefficients, ξ_j, are the interfacial shear rates on the side of the lower or upper fluid, given by

$$\left.\begin{aligned} \xi_1 &= \frac{U}{h_1}\,\frac{\lambda}{\lambda+r} - \frac{h}{\mu_1}\left(\chi + \rho_1 g_x \frac{\lambda - \delta r^2}{\lambda - r^2}\right)\frac{\lambda - r^2}{(1+r)(\lambda+r)}, \\ \xi_2 &= \frac{\xi_1}{\lambda}. \end{aligned}\right\} \tag{3.4}$$

Note that the zeroth-order velocity satisfies the no-slip and no-penetration boundary conditions at the unperturbed wall positions, $u_1^{(0)} = 0$ and $v_1^{(0)} = 0$ at $y = -h_1$, and $u_2^{(0)} = U$ and $v_2^{(0)} = 0$ at $y = h_2$. The corresponding zeroth-order pressure distribution is given by

$$p_j^{(0)}(x, y) = -\chi\, x + \rho_j g_y\, y + P_0, \tag{3.5}$$

where $g_y = -g\cos\theta_0$ is the y-component of the acceleration due to gravity, and P_0 is an unspecified constant.

Having shifted the origin of the y-axis to the position of the flat interface, we describe the profile of the uneven lower wall by the real part of the function

$$y_w(x) = -h_1 + a_W\, \mathrm{e}^{\mathrm{i}kx}, \tag{3.6}$$

where $a_W = \epsilon\, h_1$ is the wall amplitude, $\epsilon \ll 1$ is the dimensionless perturbation parameter, $\mathrm{i} = \sqrt{-1}$ is the imaginary unit, $k = 2\pi/L$ is the wavenumber, and L is the wavelength. The interface is described by the corresponding function

$$y_I(x) = a_I\, \mathrm{e}^{\mathrm{i}kx} = \epsilon\, \eta(x), \tag{3.7}$$

where $a_I = \epsilon A h_1$ is the complex interface amplitude, A is a dimensionless complex interface amplitude, and $\eta(x) = A h_1 \mathrm{e}^{\mathrm{i}kx}$ is the wave form of the perturbation. The surfactant concentration and surface tension are described by the companion functions

$$\Gamma(x) = \Gamma^{(0)} + \epsilon\, \Gamma^{(1)}(x) = \Gamma_0 + \epsilon \Gamma_1 \mathrm{e}^{\mathrm{i}kx}, \qquad \gamma(x) = \gamma^{(0)} + \epsilon\, \gamma^{(1)}(x) = \gamma_0 + \epsilon\gamma_1 \mathrm{e}^{\mathrm{i}kx}, \tag{3.8}$$

where $\Gamma^{(0)} = \Gamma_0$ and $\gamma^{(0)} = \gamma_0$ are uniform values corresponding to unidirectional flow, $\Gamma^{(1)} = \Gamma_1 \mathrm{e}^{\mathrm{i}kx}$ and $\gamma^{(1)} = \gamma_1 \mathrm{e}^{\mathrm{i}kx}$ are the first-order perturbations of Γ and γ, and Γ_1, γ_1 are complex amplitudes. Since the perturbation is small, we may write

$$\gamma_1 = -Ma\, \frac{\gamma_0}{\Gamma_0}\, \Gamma_1, \tag{3.9}$$

based on (2.4), where the Marangoni number, Ma, is defined in (2.5).

Substituting $u_j = \partial\psi_j/\partial y$ and $v_j = -\partial\psi_j/\partial x$ into (2.1), eliminating pressure and gravity by taking the curl of the resulting equation, and truncating all expressions to order of ϵ, we find that $\psi_j^{(1)}(x, y)$ are biharmonic functions, $\nabla^4 \psi_j^{(1)} = 0$. Now setting $\psi_j^{(1)} = \phi_j(\hat{y}) \exp(\mathrm{i}kx)$, where $\hat{y} = ky$, we find

$$\phi_j(\hat{y}) = a_{1j} \cosh\hat{y} + a_{2j}\hat{y}\, \cosh\hat{y} + a_{3j} \sinh\hat{y} + a_{4j}\hat{y}\, \sinh\hat{y}, \tag{3.10}$$

where a_{ij}, for $i = 1, 2, 3, 4$, $j = 1, 2$, are eight complex coefficients. The first-order pressure field can be expressed in the form

$$p_j^{(1)} = \mu_j\, q_j(\hat{y}) \exp(\mathrm{i}kx), \tag{3.11}$$

for $j = 1, 2$. Substituting this expression in the x-component of (2.1), we find

$$\mathrm{i}k\, q_j \exp(\mathrm{i}kx) = \left(\frac{\partial^3 \psi_j^{(1)}}{\partial x^2 \partial y} + \frac{\partial^3 \psi_j^{(1)}}{\partial y^3} \right), \tag{3.12}$$

yielding

$$q_j(y) = \mathrm{i}\, k^2\, (\phi_j' - \phi_j'''). \tag{3.13}$$

Kinematic compatibility requires $\mathrm{D}(y - y_I)/\mathrm{D}t = 0$, where $\mathrm{D}/\mathrm{D}t$ is the material derivative. Linearizing at steady state, we find

$$u_I \frac{\partial \eta}{\partial x} - v^{(1)}(y = 0) = 0. \tag{3.14}$$

Upon substitution, we find

$$a_{11} = -u_I h_1 A. \tag{3.15}$$

Continuity of the x and y velocity at the interface requires

$$h_1 A (\Xi_1 - \Xi_2) + a_{21} + a_{31} - a_{22} - a_{32} = 0, \qquad a_{11} = a_{12}, \tag{3.16}$$

where $\Xi_j \equiv \xi_j / k$, for $j = 1, 2$, are coefficients with dimensions of velocity. The linearized shear stress balance at the interface reads

$$\mu_2 \left(\frac{\partial u_2^{(1)}}{\partial y} + \frac{\partial v_2^{(1)}}{\partial x} \right)_{y=0} - \mu_1 \left(\frac{\partial u_1^{(1)}}{\partial y} + \frac{\partial v_1^{(1)}}{\partial x} \right)_{y=0} + (\rho_1 - \rho_2) g_x \eta(x) = -\frac{\partial \gamma^{(1)}}{\partial x}. \tag{3.17}$$

After simplification, we find

$$(a_{11} + a_{41}) - \lambda (a_{12} + a_{42}) - \frac{(\rho_1 - \rho_2)}{2\mu_1 k^2} h_1 g_x A = \frac{\mathrm{i}\gamma_1}{2\mu_1 k}. \tag{3.18}$$

The linearized normal stress balance at the interface requires

$$\left(-p_1^{(1)} + 2\mu_1 \frac{\partial v_1^{(1)}}{\partial y} \right)_{y=0} - \left(-p_2^{(1)} + 2\mu_2 \frac{\partial v_2^{(1)}}{\partial y} \right)_{y=0} - (\rho_1 - \rho_2) g_y \eta(x) = \gamma_0 \frac{\partial^2 \eta}{\partial x^2}, \tag{3.19}$$

which yields

$$-2\mathrm{i}k^2 \mu_1 a_{31} + 2\mathrm{i}k^2 \mu_2 a_{32} - (\rho_1 - \rho_2) g_y h_1 A = -\gamma_0 h_1 A k^2. \tag{3.20}$$

Note that the perturbed surfactant concentration does not enter the linearized normal stress balance, whereas the Marangoni traction appears on the right-hand side of the linearized shear stress balance (3.18).

The no-slip and no-penetration conditions at the lower and upper wall require

$$\begin{aligned} &u_2^{(1)}(y = h_2) = v_2^{(1)}(y = h_2) = v_1^{(1)}(y = -h_1) = 0, \\ &u_1^{(1)}(y = -h_1) + \left. \frac{\partial u_1^{(0)}}{\partial y} \right|_{y=-h_1} h_1 \mathrm{e}^{\mathrm{i}kx} = 0, \end{aligned} \tag{3.21}$$

yielding

$$\begin{bmatrix} \cosh \hat{h}_1 & -\hat{h}_1 \cosh \hat{h}_1 & -\sinh \hat{h}_1 & \hat{h}_1 \sinh \hat{h}_1 \\ -\sinh \hat{h}_1 & \cosh \hat{h}_1 + \hat{h}_1 \sinh \hat{h}_1 & \cosh \hat{h}_1 & -\sinh \hat{h}_1 - \hat{h}_1 \cosh \hat{h}_1 \end{bmatrix} \cdot \boldsymbol{w}_1 = \boldsymbol{b}, \tag{3.22}$$

and

$$\begin{bmatrix} \cosh \hat{h}_2 & \hat{h}_2 \cosh \hat{h}_2 & \sinh \hat{h}_2 & \hat{h}_2 \sinh \hat{h}_2 \\ \sinh \hat{h}_2 & \cosh \hat{h}_2 + \hat{h}_2 \sinh \hat{h}_2 & \cosh \hat{h}_2 & \sinh \hat{h}_2 + \hat{h}_2 \cosh \hat{h}_2 \end{bmatrix} \cdot \boldsymbol{w}_2 = \boldsymbol{0}, \tag{3.23}$$

where $\hat{h}_1 \equiv kh_1$, $\hat{h}_2 \equiv kh_2$, $\boldsymbol{w}_1 = [a_{11}, a_{21}, a_{31}, a_{41}]^T$, $\boldsymbol{w}_2 = [a_{12}, a_{22}, a_{32}, a_{42}]^T$, and

$$\boldsymbol{b} = \left[0 \quad -\frac{\chi + \rho_1 g_x}{\mu_1 k} h_1^2 - \frac{\xi_1 h_1}{k}\right]^T. \tag{3.24}$$

Finally, we linearize the surfactant transport equation for steady flow to obtain

$$u_1^{(0)} \frac{\partial \Gamma^{(1)}}{\partial x} + \Gamma^{(0)} \left(\frac{\partial u_1^{(1)}}{\partial x} + \frac{\partial u_1^{(0)}}{\partial y} \frac{\mathrm{d}\eta}{\mathrm{d}x} \right) = D_s \frac{\partial^2 \Gamma^{(1)}}{\partial x^2}, \tag{3.25}$$

where all terms are evaluated at $y = 0$. Substituting the preceding expressions in (3.25), we find that the complex amplitude of the surfactant concentration is given by

$$\frac{\Gamma_1}{\Gamma_0} = \frac{k(a_{21} + a_{31}) + \xi_1 h_1 A}{-u_I + \mathrm{i}kD_s}. \tag{3.26}$$

Equations (3.22) and (3.23) together with equations (3.9), (3.15), (3.16), (3.18), (3.20) and (3.26) constitute a system of eleven linear equations for the various complex constants introduced in the preceding analysis, including a_{ij}, A, Γ_1 and γ_1. Dimensional analysis reveals that the dimensionless complex interfacial amplitude, A, depends on the reduced lower film thickness, h_1/d, reduced wavelength, L/d, viscosity ratio, λ, density ratio, δ, channel inclination angle, θ_0, Marangoni number, Ma, capillary numbers

$$Ca_\xi \equiv \frac{\mu_1 \xi_1 h_1}{\gamma_0}, \qquad Ca_\chi \equiv \frac{\chi h_1^2}{\gamma_0}, \qquad Ca_g \equiv \frac{\rho_1 g h_1^2}{\gamma_0}, \tag{3.27}$$

and property group

$$\alpha \equiv \frac{\gamma_0 h_1}{\mu_1 D_s}, \tag{3.28}$$

expressing the surfactant diffusivity. Alternative dimensionless parameters can be defined by choosing different velocity and length scales, as the need arises.

3.1. *Results and discussion*

First, we consider shear-driven flow in a horizontal channel with neutrally buoyant fluids, setting $Ca_\chi = 0$, $Ca_g = 0$, $\theta_0 = 0$ and $\delta = 1$. To isolate the effect of the shear flow determined by the upper-wall velocity, U, we introduce the alternative capillary number

$$Ca = \frac{\mu_1 U}{\gamma_0}. \tag{3.29}$$

Raising Ca while holding all other dimensionless parameters fixed amounts to increasing the velocity of the upper wall driving the fluid motion while holding all other physical and geometrical variables constant.

We begin by considering flow in the absence of a surfactant, setting the Marangoni number to zero. Figure 2(a, b) illustrates the effect of the reduced lower film thickness, h_1/L, on the amplitude and phase shift of the interfacial wave for $Ca = \infty$ (heavy line), 50, 5, 2, 1, 0.2 and 0.05, $L/d = 1$, and viscosity ratio $\lambda = 0.2$ and 2. The curves for $Ca = 50$ are visually indistinguishable from the curves for $Ca = \infty$ wherein the interface is free to deform under the influence of the perturbation flow induced by the wall corrugations unrestricted by surface tension. In all cases, as the film thickness h_1/L is reduced, the amplitude of the interface tends to the amplitude of the

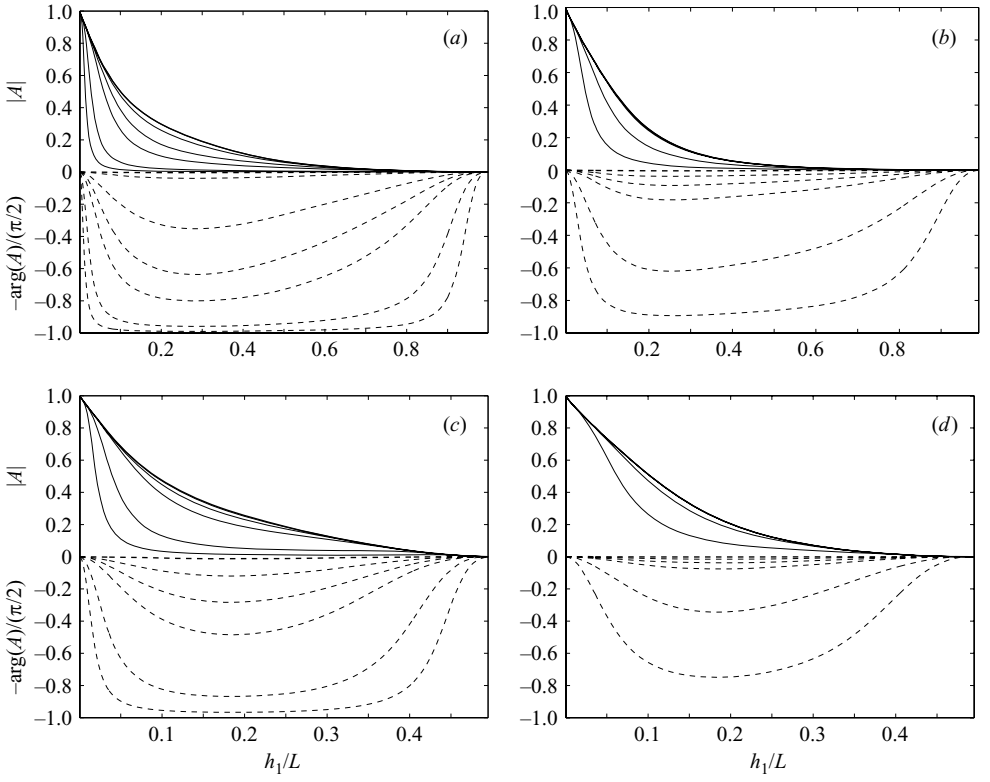

FIGURE 2. Amplitude and phase shift of the interfacial wave as predicted by the linear perturbation analysis for a sinusoidal wall in the absence of surfactants. The graphs illustrate the effect of lower film thickness, h_1/L, on the amplitude (solid lines) and phase shift (dashed lines) of the interfacial wave with respect to the wavy wall, for $Ca = \infty$ (heavy lines), 50, 5, 2, 1, 0.2, 0.05 and (*a*) $L/d = 1$, $\lambda = 0.2$, (*b*) $L/d = 1$, $\lambda = 2$, (*c*) $L/d = 2$, $\lambda = 0.2$, (*d*) $L/d = 2$, $\lambda = 2$. Note that some curves for large capillary numbers are indistinguishable.

lower wall, $|A| \to 1$, the phase shift $\arg(A)$ tends to zero, and the interface tends to conform geometrically with the wavy wall. On the other hand, as the film thickness is increased, the amplitude of the interface decreases in a monotonic fashion and tends to vanish as the interface approaches the upper wall. Correspondingly, the phase shift rises from the value of zero, reaches a maximum value in the range $(0, \pi/2)$, and finally drops down to zero as the interface approaches the upper wall. A compelling physical reason as to why an interface located near the upper wall is nearly in-phase with the corrugations of the lower wall is not apparent. In the case of flow with negligible capillary forces, $Ca = \infty$, the phase shift is zero for any film thickness, and the interface is always in phase with the lower wall.

Figure 2(c, d) describes the deformation of the interface for conditions that are identical to those corresponding to figure 2(a, b), except that the period of the undulations is twice the clearance of the channel, $L/d = 2$. Comparing the bold curves in the upper and lower frames corresponding to the capillary number $Ca = \infty$, we find that the the effect of the wavy wall becomes increasingly important as the reduced wavelength L/d becomes higher. Physically, the perturbation flow induced by the corrugations decays over a length scale that is comparable to the period of the sinusoidal wall, as evidenced by the solution for the streamfunction shown in (3.10).

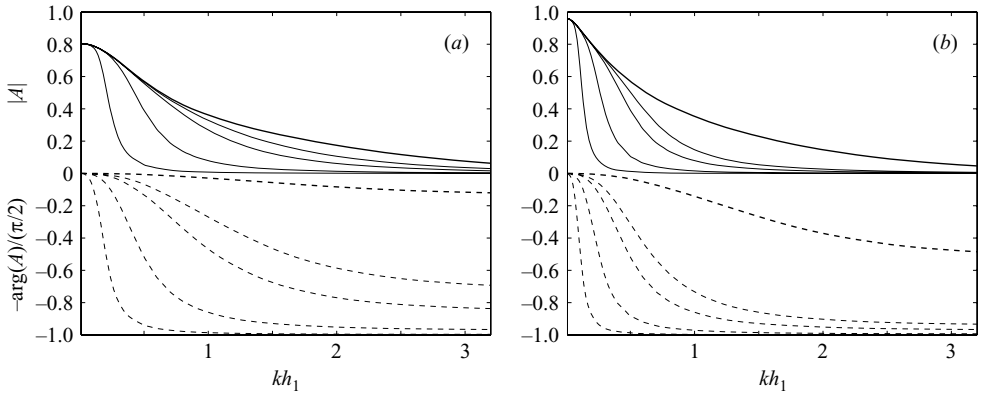

FIGURE 3. Effect of the reduced wavenumber, kh_1, on the magnitude (solid lines) and phase shift (dashed lines) of the interfacial wave for $\lambda = 0.2$, $Ca_\xi = 10$ (heavy lines), 1, 0.5, 0.1, 0.01, and (*a*) $h_1/d = 0.1$, (*b*) $h_1/d = 0.02$.

The flow with $L/d = 1$ approximates semi-infinite shear flow over a wavy wall well when the interface is located within a substantial portion of the channel away from the upper wall.

Figure 3 illustrates the effect of the wavelength expressed by the reduced wavenumber, kh_1, for $Ma = 0$, $\lambda = 0.2$, and lower film thickness $h_1/d = 0.1$ or 0.02. The various curves correspond to capillary number $Ca_\xi = 10$, 1, 0.5, 0.1 and 0.01, defined with respect to the shear rate at the unperturbed interface in unidirectional flow. Physically, raising Ca_ξ is tantamount to reducing the interfacial tension while holding all other parameters constant. As the wavelength of the corrugations is raised and correspondingly the wavenumber tends to zero, the amplitude of the interface approaches a certain limiting value and the phase shift tends to zero. As the interface moves farther from the upper wall, $h_1/d \to 0$, the limiting value of the amplitude is shifted upward toward unity. In the long-wave limit, the two-layer flow can be described by the equations of lubrication flow resulting in a coupled system of ordinary differential equations (Blyth & Pozrikidis 2004*a*). On the other hand, as the wavenumber is raised, the amplitude of the interfacial wave decreases monotonically, whereas the phase shift initially increases and then plateaus to a value that is less than $\pi/2$.

Next, we address the effect of an insoluble surfactant. Figure 4 illustrates the effect of a non-diffusive surfactant, $D_s = 0$, for a flow with comparable viscous and capillary stresses, $Ca_\xi = 1$, $h_1/d = 0.2$ and $\lambda = 0.2$, over a broad range of Marangoni numbers. The graphs drawn with the solid lines in figure 4(*a*) reveal that the surfactant acts to increase the amplitude of the interface. The effect is most pronounced at low and moderate wavenumbers, $kh_1 < 1.5$. A similar effect was reported by Pozrikidis (2003) for film flow down an inclined wavy wall at vanishing Reynolds number. The graphs drawn with the dashed lines in figure 4(*a*) show that the phase shift is negative for low wavenumbers and positive for higher wavenumbers. As the Marangoni number is raised, the wavenumber where the effect of the surfactant is most important is shifted to lower values.

Figure 4(*b*) illustrates the properties of the surfactant concentration wave, showing that raising the Marangoni number reduces the amplitude and increases the phase shift. A reduction in the amplitude does not necessarily imply that the effect of the surfactant becomes weaker, as the surface tension becomes more sensitive to the

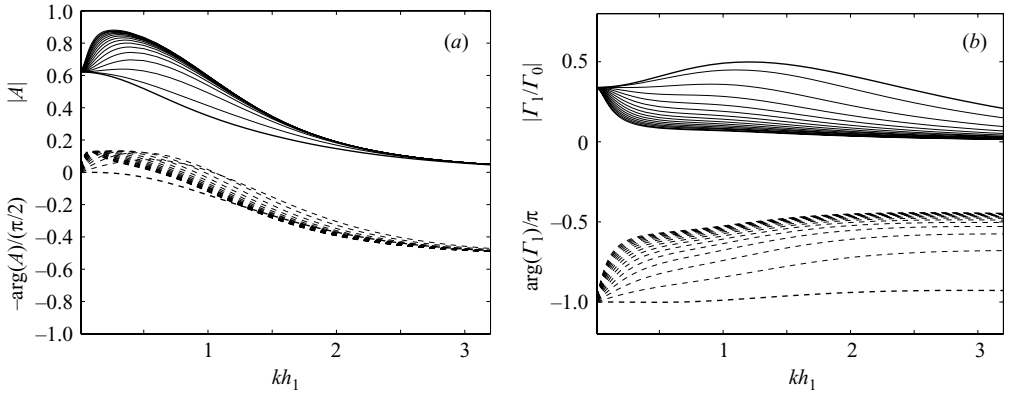

FIGURE 4. Predictions of linear perturbation theory in the presence of a non-diffusive surfactant for $h_1/d = 0.2$, $\lambda = 0.2$, $Ca_\xi = 1$, $Ma = 0$ (heavy lines), 1, 2, ..., 15. (*a*) Magnitude (solid lines) and phase shift (dashed lines) of the interfacial wave. (*b*) Magnitude (solid lines) and phase shift (dashed lines) of the surfactant concentration wave. The phase-shifts, arg(A) and arg(Γ_1), have been reduced by $\pi/2$ and π, respectively.

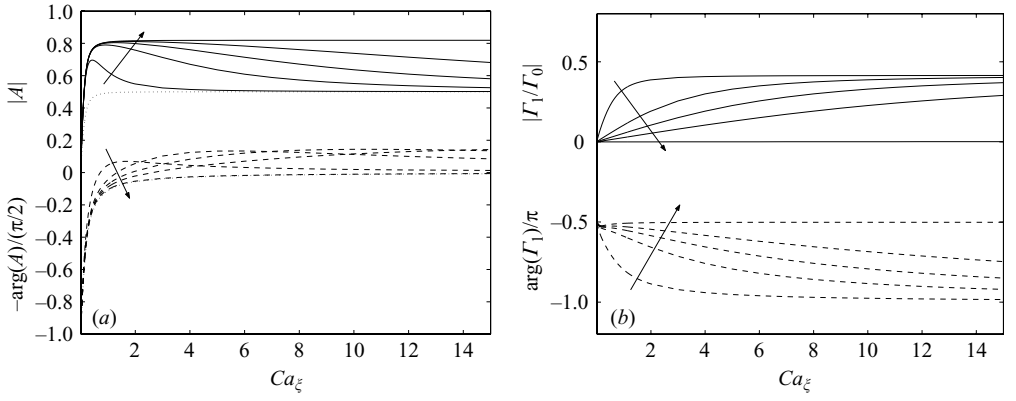

FIGURE 5. Predictions of linear perturbation theory for $h_1/d = 0.1$, $L/d = 1$, $\lambda = 0.2$, $D_s = 0$ and $Ma = 1, 5, 10, 20, \infty$. The curves for $Ma = 0$ are shown as dotted lines. (*a*) Magnitude (solid lines) and phase shift (dashed lines) of the interfacial wave. (*b*) Magnitude (solid lines) and phase shift (dashed lines) of the surfactant concentration wave. The arrows point in the direction of Ma increasing from 1 to ∞.

surfactant concentration when the Marangoni number is raised. As the wavenumber tends to zero, the reduced amplitude, $|\Gamma_1/\Gamma_0|$, approaches a constant value independent of the Marangoni number, while the phase shift, arg(Γ_1), approaches the value $-\pi$, revealing that the perturbation of the surfactant concentration tends to become out of phase with respect to the corrugations of the lower wall. On the other hand, as the wavenumber is raised, the phase shift of the surfactant concentration increases monotonically, whereas the amplitude behaves in a way that is determined by the Marangoni number. At high Marangoni numbers, the ratio $|\Gamma_1/\Gamma_0|$ decreases monotonically with kh_1, whereas at low Marangoni numbers, a maximum appears at certain wavenumbers.

Figure 5(*a*) illustrates the effect of the non-diffusive surfactant on a thin film, $h_1/d = 0.1$, $L/d = 1$, $\lambda = 0.2$, over a range of capillary numbers, Ca_ξ. The dotted

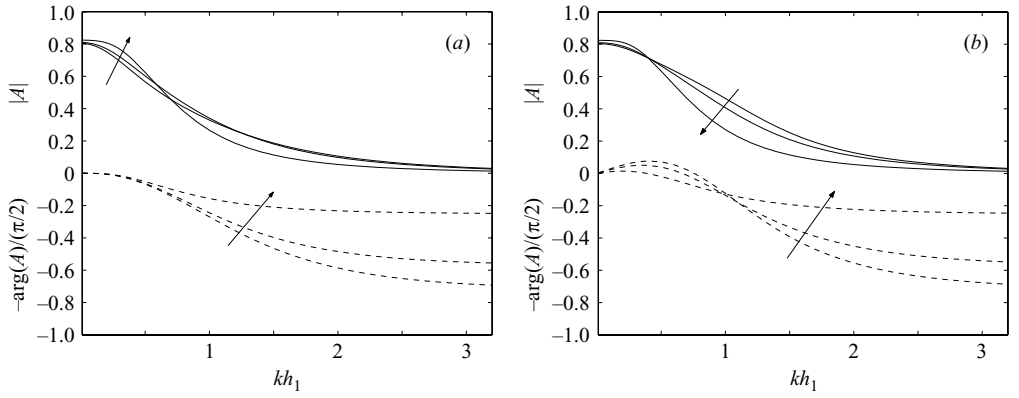

FIGURE 6. Predictions of linear theory for the magnitude (solid lines) and phase shift (dashed lines) of the interfacial wave for a flow with $h_1/d = 0.1$, $Ca_\xi = 1$, viscosity ratio $\lambda = 0.2$, 1, 5, and Marangoni number (*a*) $Ma = 0$, and (*b*) 1. The arrows point in the direction of increasing λ.

lines describe the behaviour in the absence of a surfactant, $Ma = 0$, showing that the amplitude of the interface increases and the phase shift decreases monotonically as the capillary number is raised. When surfactant is introduced, the monotonic growth is replaced by an overshooting followed by decay to an asymptotic limit. When $Ma = 1$, the interface amplitude peaks when $Ca_\xi \approx 0.3$ at an amplitude that is about 57 % higher than that in the absence of the surfactant. The phase shift reaches the minimum value of $\arg(A) = -0.035\pi$ when $Ca_\xi \approx 1.7$. The graphs show that the effect of the surfactant is most important at intermediate capillary numbers and less significant at low and high capillary numbers. As the Marangoni number is raised, the tail of the amplitude graph moves upward and the influence of the surfactant becomes significant over a broader range of capillary numbers. As Ma tends to the theoretical limit of infinity, the amplitude curve obtains a limiting shape where the surfactant has a nearly uniform effect for capillary numbers $Ca_\xi > 2$. In this range, the amplitude of the interface is elevated by approximately 64 % with respect to that in the absence of surfactant. The precise shape of the phase-shift graph depends on the Marangoni number. The curve for $Ma = \infty$ nearly coincides with that for $Ma = 0$.

Figure 5(*b*) illustrates the behaviour of the surfactant concentration wave established in response to the wavy wall. As the capillary number is raised, the reduced amplitude described by the solid lines increases from zero to a certain value underneath 0.5, while the phase shift decreases monotonically from the value of $-\pi/2$. As the Marangoni number is raised, the amplitude of the surfactant concentration wave tends to zero, while the phase shift tends to $-\pi/2$. In this limit, the surfactant is distributed nearly uniformly over the interface. However, the small gradient of the surfactant concentration is multiplied by a large coefficient to yield non-infinitesimal Marangoni tensions.

Figure 6 illustrates the effect of the viscosity ratio on the amplitude of the interface for a specified capillary number. The graphs in figure 6(*a*) for a clean interface show that the amplitude of long waves for $\lambda = 0.2$ is smaller than that for $\lambda = 1$, whereas the amplitude of short waves is higher than that for $\lambda = 1$. For $\lambda = 5$, the converse behaviour is observed. The phase shift for $\lambda = 0.2$ is uniformly higher than that for $\lambda = 1$, whereas the phase shift for $\lambda = 5$ is uniformly lower than that for $\lambda = 1$. The graphs in figure 6(*b*) for $Ma = 1$ show that the surfactant modifies both the amplitude

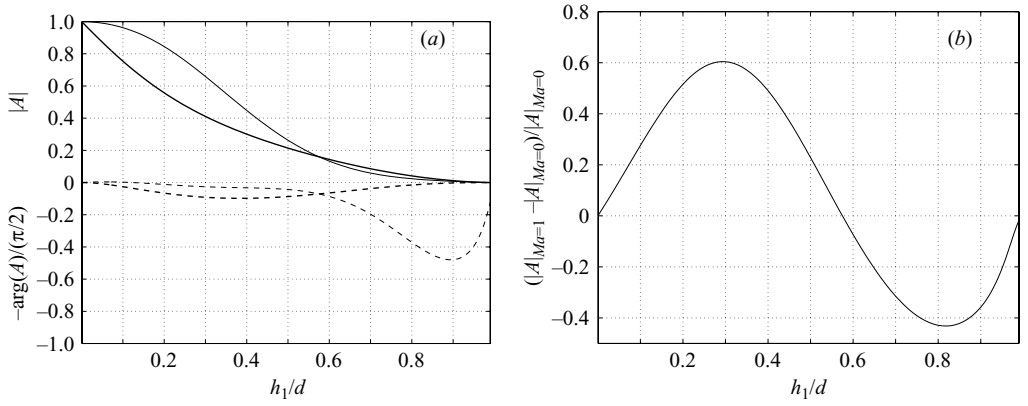

FIGURE 7. Predictions of linear theory for $L/d = 3$, $Ca = 1$, $\lambda = 0.5$ and $D_s = 0$. (*a*) Magnitude (solid lines) and phase shift (dashed lines) of the surface wave for $Ma = 0$ (heavy lines) and 5 (thin lines), and (*b*) relative change in the magnitude, $(|A|_{Ma=1} - |A|_{Ma=0}) / |A|_{Ma=0}$.

and phase-shift response curves significantly when the viscosity ratio is less than unity. As the viscosity ratio is reduced, the critical wavenumber defined by the intersection of the current with the $\lambda = 1$ curve shifts toward lower values. In the low-wavenumber region, the phase shift for $\lambda = 0.2$ is negative and lower than that for $\lambda = 1$ and 5.

The effect of the surfactant is further illustrated in figure 7(*a*) where the amplitude and phase shift of the interfacial wave are plotted with respect to the lower film thicknesses, h_1/d for $L/d = 3$, $D_s = 0$, $\lambda = 0.5$, $Ca = 1$ and $Ma = 0$ or 5. Introducing surfactant increases the amplitude of the interface and reduces the phase shift for low thicknesses, h_1/d, but the trend is reversed when h_1/d becomes sufficiently high. As the interface approaches the upper wall, the phase shift for $Ma = 5$ retains a significant positive value before finally sharply dropping to zero. The solid curves for the amplitude and the broken curves for the phase shift for $Ma = 0$ and 5 cross at the same critical value $(h_1/d)_c$; at this value, adding surfactant has no effect on the deformation of the interface. Figure 7(*b*) shows a graph of the relative change in the interface amplitude expressed by the ratio $(|A|_{Ma=1} - |A|_{Ma=0}) / |A|_{Ma=0}$. A maximum of 60 % is observed at $h_1/d \approx 0.3$, and a minimum of −42 % is observed at $h_1/d \approx 0.8$. Calculations with different sets of parameters have shown that the critical value, $(h_1/d)_c$, is independent of the Marangoni and capillary numbers, though it depends on the viscosity ratio and reduced wavelength, L/d. When $\lambda = 1$, the critical value is exactly 0.5 for any reduced wavelength L/d; when $\lambda < 1$, the critical value is greater than 0.5 and increases as L/d is raised; and when $\lambda > 1$, the critical h_1/d is less than 0.5 and decreases as L/d is raised.

Surface diffusion ameliorates the effect of an insoluble surfactant by distributing the molecules more uniformly over the interface, and thereby reducing the Marangoni traction. Figure 8 illustrates the effect for a typical case with $\alpha = \infty$ (vanishing diffusivity), 5, 2, 1 and 1/3. The graphs in figure 8(*a*) confirm that increasing the surfactant diffusivity reduces the interface amplitude while also increasing the phase shift. In effect, increasing the surfactant diffusivity has the same influence as reducing the Marangoni number. A fast diffusing surfactant alters the surface tension uniformly over the interface and effectively shifts the capillary number into a value that is determined by the *a priori* unknown arclength of the interface over each period. As the surfactant diffusivity is increased, both the amplitude and phase shift of

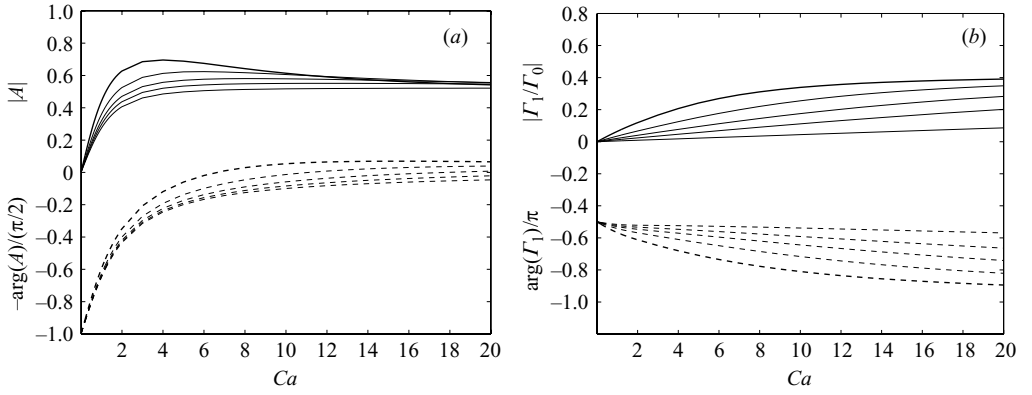

FIGURE 8. Effect of surfactant diffusivity for $h_1/d = 0.1$, $L/d = 1$, $\lambda = 0.2$, $Ma = 1$ and $\alpha = \infty$ (heavy lines), 5, 2, 1, 1/3. (*a*) Magnitude (solid lines) and phase shift (dashed lines) of (*a*) the surface wave, and (*b*) the surfactant concentration wave.

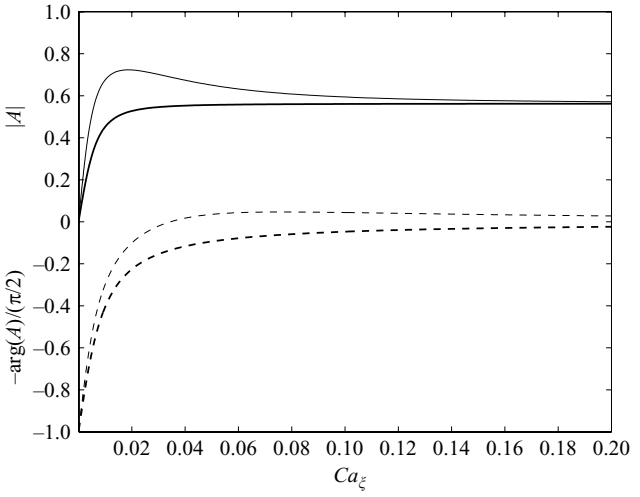

FIGURE 9. Predictions of linear theory for the magnitude (solid lines) and phase shift (dashed lines) of the surface wave in pressure-driven flow with $U = 0$, $h_1/d = 0.1$, $L/d = 1$, $\lambda = 0.2$, $D_s = 0$, $Ma = 0$ (heavy lines) and 1 (thin lines).

the surfactant concentration wave decrease by a substantial amount, as shown in figure 8(*b*).

Additional calculations have shown that the shape of the interface in pressure- and gravity-driven flow is similar to that in shear-driven flow discussed in this section. As an example, figure 9 shows the effect of the surfactant over a range of the capillary numbers, Ca_χ, for a typical flow configuration. The graphs displayed are similar to those shown in figure 5(*a*) for shear-driven flow. As we have already seen, the effect of the surfactant is most pronounced for intermediate capillary numbers.

4. Boundary integral method for arbitrary wall geometry

In the second part of the investigation, we use numerical methods to track the evolution of the interface from a specified initial configuration over a wall with

arbitrary geometry, as depicted in figure 1(*a*). The main objective is to capture the interfacial shape after a steady state has been established, and thereby confirm and extend the predictions of the linear perturbation analysis undertaken in § 3 for a small-amplitude sinusoidal wall. A second objective is to describe the structure of the flow over walls with indented topography.

4.1. *Boundary-integral formulation*

In the inclined system of coordinates depicted in figure 1(*a*), the lower wall is described by the periodic function $y = y_w(x)$, and the upper wall is located at $y = d$. To develop the boundary-integral formulation for periodic flow, we decompose the velocity, $\boldsymbol{u}$, and pressure, p, within each fluid into a reference component denoted by the superscript R, and a complementary disturbance component denoted by the superscript D,

$$\boldsymbol{u} = \boldsymbol{u}^R + \boldsymbol{u}^D, \qquad p = p^R + p^D. \tag{4.1}$$

The reference flow satisfies the equations of Stokes flow with the gravitational body force included, while the disturbance flow satisfies the unforced equations of Stokes flow. To simplify the formulation, we stipulate that the disturbance flow does not induce a pressure drop over each period.

A suitable choice for the reference velocity corresponds to unidirectional flow with velocity components

$$u_x^{R^{(j)}} = \frac{U}{d}\, y + \frac{\chi + \rho_j g_x}{2\,\mu_j}\, y\,(d - y), \qquad u_y^{R^{(j)}} = 0, \tag{4.2}$$

for $j = 1, 2$. The associated reference pressure field is given by

$$p^{R^{(j)}} = -\chi\, x + \rho_j\, g_y\, y + P_j, \tag{4.3}$$

where P_j are constants. Since the reference velocity satisfies the no-slip boundary condition at the upper wall, $u_x^{R^{(2)}}(y = d) = U$, the disturbance velocity is required to vanish at the upper wall,

$$u_x^{D^{(2)}}(y = d) = 0, \qquad u_y^{D^{(2)}}(y = d) = 0. \tag{4.4}$$

Imposing the zero velocity condition at the lower wall, we find

$$\left.\begin{aligned} u_x^{D^{(1)}}(y = y_w(x)) &= -u_x^{R^{(1)}}(y = y_w(x)), \\ u_y^{D^{(1)}}(y = y_w(x)) &= 0. \end{aligned}\right\} \tag{4.5}$$

At the interface, the reference velocity undergoes a discontinuity given by

$$\left.\begin{aligned} \Delta u_x^R \equiv u_x^{R^{(1)}} - u_x^{R^{(2)}} &= \frac{1}{2\mu_1}\left[\chi\,\left(1 - \frac{1}{\lambda}\right) + \rho_1 g_x \left(1 - \frac{\delta}{\lambda}\right)\right]\, y\,(d - y), \\ \Delta u_y^R \equiv u_y^{R^{(1)}} - u_y^{R^{(2)}} &= 0, \end{aligned}\right\} \tag{4.6}$$

where $\lambda = \mu_2/\mu_1$ is the viscosity ratio and $\delta = \rho_2/\rho_1$ is the density ratio. The interfacial traction of the reference flow also undergoes a discontinuity given by

$$\begin{aligned} \Delta \boldsymbol{f}^R \equiv \left(\boldsymbol{\sigma}^{R^{(1)}} - \boldsymbol{\sigma}^{R^{(2)}}\right)\cdot \boldsymbol{n} &= -(P_1 - P_2)\boldsymbol{n} \\ &+ \left[\begin{array}{cc} -\Delta\rho g_y y & \big|\ \mu_1(1-\lambda)\xi - \Delta\rho g_x (y - d/2) \\ \mu_1(1-\lambda)\xi - \Delta\rho g_x (y - d/2)\ \big| & -\Delta\rho g_y y \end{array}\right]\cdot \boldsymbol{n}, \end{aligned} \tag{4.7}$$

where $\Delta\rho = \rho_1 - \rho_2 = \rho_1\,(1-\delta)$ and $\xi = U/d$. The disturbance traction undergoes a corresponding discontinuity given by

$$\Delta \boldsymbol{f}^{D} = -\gamma\,\kappa\,\boldsymbol{n} - \boldsymbol{t}\,\frac{\partial \gamma}{\partial l} - \Delta \boldsymbol{f}^{R}. \tag{4.8}$$

To facilitate the notation, we introduce the single- and double-layer Stokes flow potentials defined on a line C,

$$\mathscr{I}_j^{SLP}(\boldsymbol{x}_0,\, \boldsymbol{f}; C) \equiv \frac{1}{4\pi\mu_1}\int_C G_{ij}(\boldsymbol{x}, \boldsymbol{x}_0)\, f_i(\boldsymbol{x})\, \mathrm{d}l(\boldsymbol{x}), \tag{4.9}$$

and

$$\mathscr{I}_j^{DLP}(\boldsymbol{x}_0,\, \boldsymbol{u}; C) \equiv \frac{1}{4\pi}\int_C u_i(\boldsymbol{x})\, T_{ijk}(\boldsymbol{x}, \boldsymbol{x}_0)\, n_k(\boldsymbol{x})\, \mathrm{d}l(\boldsymbol{x}), \tag{4.10}$$

where G_{ij} is the periodic velocity Green's function of two-dimensional Stokes flow representing the flow induced by a periodic array of point forces in a semi-infinite domain bounded by the upper wall, and T_{ijk} is the associated stress tensor.

Applying the boundary-integral formulation for the disturbance flow in the lower fluid at a point $\boldsymbol{x}_0$ located at the interface (e.g. Pozrikidis 1992, 2002), we obtain the integral representation

$$\begin{aligned}\tfrac{1}{2}\,u_j^{D^{(1)}}(\boldsymbol{x}_0) = &-\mathscr{I}_j^{SLP}\big(\boldsymbol{x}_0,\, \boldsymbol{f}^{D^{(1)}}; I,\, C_L^{(1)},\, C_R^{(1)} + W\big)\\ &+ \check{\mathscr{I}}_j^{DLP}\big(\boldsymbol{x}_0,\, \boldsymbol{u}^{D^{(1)}},\, I\big) + \mathscr{I}_j^{DLP}\big(\boldsymbol{x}_0,\, \boldsymbol{u}^{D^{(1)}}; C_L^{(1)},\, C_R^{(1)},\, W\big),\end{aligned} \tag{4.11}$$

where I denotes one period of the interface, W denotes one period of the lower wall, $C_L^{(1)}$ and $C_R^{(1)}$ are the left and right periodic segments depicted in figure 1(*a*), and $\check{\mathscr{I}}^{DLP}$ denotes the principal value of the double-layer potential. The unit normal vector, $\boldsymbol{n}$, points into the control volume enclosed by one period of the flow, as shown in figure 1(*a*). Because of the periodicity of the Green's function and disturbance flow, the contribution of the double-layer potential from the left and right periodic segments is zero due to cancellation. Invoking our earlier stipulation that the disturbance flow does not induce a pressure drop over one period, we find that the corresponding contribution of the single-layer potential is also zero due to cancellation, and derive the simplified representation

$$\begin{aligned}\tfrac{1}{2}\,u_j^{D^{(1)}}(\boldsymbol{x}_0) = &-\mathscr{I}_j^{SLP}\big(\boldsymbol{x}_0,\, \boldsymbol{f}^{D^{(1)}}; I\big) - \mathscr{I}_j^{SLP}\big(\boldsymbol{x}_0,\, \boldsymbol{f}^{D^{(1)}}; W\big)\\ &+ \check{\mathscr{I}}_j^{DLP}\big(\boldsymbol{x}_0,\, \boldsymbol{u}^{D^{(1)}}; I\big) + \mathscr{I}_j^{DLP}\big(\boldsymbol{x}_0,\, \boldsymbol{u}^{D^{(1)}}; W\big).\end{aligned} \tag{4.12}$$

Repeating the derivation for the upper fluid, keeping in mind that the normal vector over the interface is directed into the lower fluid and the velocity Green's function is zero over the upper wall, we find

$$\tfrac{1}{2}\,u_j^{D^{(2)}}(\boldsymbol{x}_0) = \frac{1}{\lambda}\,\mathscr{I}_j^{SLP}\big(\boldsymbol{x}_0,\, \boldsymbol{f}^{D^{(2)}}; I\big) - \check{\mathscr{I}}_j^{DLP}\big(\boldsymbol{x}_0,\, \boldsymbol{u}^{D^{(2)}}; I\big). \tag{4.13}$$

Next, we multiply (4.13) by the viscosity ratio λ, and add the result to (4.12) to find

$$\begin{aligned}\tfrac{1}{2}\,\big[u_j^{D^{(1)}} + \lambda\, u_j^{D^{(2)}}\big](\boldsymbol{x}_0) = &-\mathscr{I}_j^{SLP}\big(\boldsymbol{x}_0,\, \Delta\boldsymbol{f}^{D}; I\big) - \mathscr{I}_j^{SLP}\big(\boldsymbol{x}_0,\, \boldsymbol{f}^{D^{(1)}}; W\big)\\ &+ \check{\mathscr{I}}_j^{DLP}\big(\boldsymbol{x}_0,\, \boldsymbol{u}^{D^{(1)}} - \lambda\,\boldsymbol{u}^{D^{(2)}}; I\big) + \mathscr{I}_j^{DLP}\big(\boldsymbol{x}_0,\, \boldsymbol{u}^{D^{(1)}}; W\big).\end{aligned} \tag{4.14}$$

Continuity of velocity at the interface requires

$$\boldsymbol{u}^{D^{(2)}} = \boldsymbol{u}^{D^{(1)}} + \Delta \boldsymbol{u}^R. \tag{4.15}$$

Using this relation to eliminate $u_j^{D^{(2)}}(\boldsymbol{x}_0)$ in favour of $u_j^{D^{(1)}}(\boldsymbol{x}_0)$ from (4.14), and rearranging, we obtain

$$\begin{aligned}\frac{1+\lambda}{2}\, u_j^{D^{(1)}}(\boldsymbol{x}_0) = &-\tfrac{1}{2}\lambda\, \Delta u_j^R(\boldsymbol{x}_0) - \mathscr{I}_j^{SLP}(\boldsymbol{x}_0, \Delta \boldsymbol{f}^D; I) \\ &-\mathscr{I}_j^{SLP}\big(\boldsymbol{x}_0, \boldsymbol{f}^{D^{(1)}}; W\big) + (1-\lambda)\, \check{\mathscr{I}}_j^{DLP}\big(\boldsymbol{x}_0, \boldsymbol{u}^{D^{(1)}}; I\big) \\ &-\lambda\, \check{\mathscr{I}}_j^{DLP}(\boldsymbol{x}_0, \Delta \boldsymbol{u}^R; I) + \mathscr{I}_j^{DLP}\big(\boldsymbol{x}_0, \boldsymbol{u}^{D^{(1)}}; W\big).\end{aligned} \tag{4.16}$$

Transferring the terms involving the unknown disturbance wall traction and interfacial velocity to the left-hand side and rearranging, we find

$$\begin{aligned}&\mathscr{I}_j^{SLP}\big(\boldsymbol{x}_0, \boldsymbol{f}^{D^{(1)}}; W\big) - (1-\lambda)\, \check{\mathscr{I}}_j^{DLP}\big(\boldsymbol{x}_0, \boldsymbol{u}^{D^{(1)}}; I\big) + \frac{1+\lambda}{2}\, u_j^{D^{(1)}}(\boldsymbol{x}_0) \\ &= \mathscr{I}_j^{DLP}\big(\boldsymbol{x}_0, \boldsymbol{u}^{D^{(1)}}; W\big) - \mathscr{I}_j^{SLP}(\boldsymbol{x}_0, \Delta \boldsymbol{f}^D; I) - \lambda\, \big(\tfrac{1}{2}\, \Delta u_j^R(\boldsymbol{x}_0) + \check{\mathscr{I}}_j^{DLP}(\boldsymbol{x}_0, \Delta \boldsymbol{u}^R; I)\big).\end{aligned} \tag{4.17}$$

Next, we apply the boundary-integral representation for the disturbance flow in the lower fluid and the reciprocal theorem of Stokes flow in the upper fluid at a point $\boldsymbol{x}_0$ located at the lower wall, W, and obtain

$$\begin{aligned}\tfrac{1}{2}\, u_j^{D^{(1)}}(\boldsymbol{x}_0) = &-\mathscr{I}_j^{SLP}\big(\boldsymbol{x}_0, \boldsymbol{f}^{D^{(1)}}; I\big) - \mathscr{I}_j^{SLP}\big(\boldsymbol{x}_0, \boldsymbol{f}^{D^{(1)}}; W\big) \\ &+ \mathscr{I}_j^{DLP}\big(\boldsymbol{x}_0, \boldsymbol{u}^{D^{(1)}}; I\big) + \check{\mathscr{I}}_j^{DLP}\big(\boldsymbol{x}_0, \boldsymbol{u}^{D^{(1)}}; W\big),\end{aligned} \tag{4.18}$$

and

$$0 = \mathscr{I}_j^{SLP}\big(\boldsymbol{x}_0, \boldsymbol{f}^{D^{(2)}}; I\big) - \lambda\, \mathscr{I}_j^{DLP}\big(\boldsymbol{x}_0, \boldsymbol{u}^{D^{(2)}}; I\big). \tag{4.19}$$

The second equation can be restated as

$$0 = \mathscr{I}_j^{SLP}\big(\boldsymbol{x}_0, \boldsymbol{f}^{D^{(2)}}; I\big) - \lambda\, \mathscr{I}_j^{DLP}\big(\boldsymbol{x}_0, \boldsymbol{u}^{D^{(1)}}; I\big) - \lambda\, \mathscr{I}_j^{DLP}(\boldsymbol{x}_0, \Delta \boldsymbol{u}^R, I). \tag{4.20}$$

Adding (4.18) and (4.20), we find

$$\begin{aligned}\tfrac{1}{2}\, u_j^{D^{(1)}}(\boldsymbol{x}_0) = &-\mathscr{I}_j^{SLP}\big(\boldsymbol{x}_0, \Delta \boldsymbol{f}^D, I\big) - \mathscr{I}_j^{SLP}\big(\boldsymbol{x}_0, \boldsymbol{f}^{D^{(1)}}, W\big) \\ &+ (1-\lambda)\, \mathscr{I}_j^{DLP}\big(\boldsymbol{x}_0, \boldsymbol{u}^{D^{(1)}}; I\big) - \lambda\, \mathscr{I}_j^{DLP}(\boldsymbol{x}_0, \Delta \boldsymbol{u}^R; I) + \check{\mathscr{I}}_j^{DLP}(\boldsymbol{x}_0, \boldsymbol{u}^{D^{(1)}}; W).\end{aligned} \tag{4.21}$$

Transferring the unknowns to the left-hand side, we find

$$\begin{aligned}&\mathscr{I}_j^{SLP}\big(\boldsymbol{x}_0, \boldsymbol{f}^{D^{(1)}}, W\big) - (1-\lambda)\, \mathscr{I}_j^{DLP}\big(\boldsymbol{x}_0, \boldsymbol{u}^{D^{(1)}}, I\big) \\ &= \check{\mathscr{I}}_j^{DLP}\big(\boldsymbol{x}_0, \boldsymbol{u}^{D^{(1)}}, W\big) - \tfrac{1}{2}\, u_j^{D^{(1)}}(\boldsymbol{x}_0) - \mathscr{I}_j^{SLP}\big(\boldsymbol{x}_0, \Delta \boldsymbol{f}^D, I\big) - \lambda\, \mathscr{I}_j^{DLP}(\boldsymbol{x}_0, \Delta \boldsymbol{u}^R, I).\end{aligned} \tag{4.22}$$

Equations (4.17) and (4.22) comprise a system of integral equations for the unknown functions $\boldsymbol{f}^{D^{(1)}}$ and $\boldsymbol{u}^{D^{(1)}}$.

4.2. *Numerical method*

To solve the integral equations, we discretize one period of the lower wall into N_w elements and one period of the film surface into N_s elements, introduce approximations for the unknown functions over the elements, and apply the integral equations at wall and surface element collocation points to obtain a system of linear algebraic

equations (e.g. Pozrikidis 2002). In the present implementation, the components of the disturbance velocity and traction are approximated with constant functions over each element, and the integral equation is enforced at collocation points located at the element mid-points, yielding the linear system

$$\boldsymbol{A}^{WW}\cdot\boldsymbol{f}^{DW}-(1-\lambda)\,\boldsymbol{B}^{WI}\cdot\boldsymbol{u}^{D1I} = \boldsymbol{B}^{WW}\cdot\boldsymbol{u}^{DW}-\tfrac{1}{2}\,\boldsymbol{u}^{DW}-\boldsymbol{A}^{WI}\cdot\Delta\boldsymbol{f}^{DI}-\lambda\,\boldsymbol{B}^{WI}\cdot\Delta\boldsymbol{u}^{RI} \quad (4.23)$$

for the wall elements originating from (4.22), and the companion linear system

$$\boldsymbol{A}^{IW}\cdot\boldsymbol{f}^{DW}-(1-\lambda)\boldsymbol{B}^{II}\cdot\boldsymbol{u}^{D1I}+\frac{1+\lambda}{2}\,\boldsymbol{u}^{D1I} = \boldsymbol{B}^{IW}\cdot\boldsymbol{u}^{DW}-\boldsymbol{A}^{II}\cdot\Delta\boldsymbol{f}^{DI}-\lambda\left(\tfrac{1}{2}\,\Delta\boldsymbol{u}^{RI}+\boldsymbol{B}^{II}\cdot\Delta\boldsymbol{u}^{RI}\right) \quad (4.24)$$

for the interfacial elements originating from (4.17). The vector $\boldsymbol{f}^{DW}$ contains the x-components of the disturbance wall traction followed by the y-components, and the vector $\boldsymbol{u}^{DW}$ contains the x-components of the disturbance wall velocity followed by the y-components. The components of the remaining vectors and the union of the $2N_w$ scalar equations encapsulated in (4.23) and $2N_s$ scalar equations encapsulated in (4.24) are arranged in a similar fashion. The influence matrices introduced in (4.23) and (4.24) are defined in terms of integrals of the single- and double-layer potential over the boundary elements. The size of the matrices in the sets $\boldsymbol{A}^{WW}$, $\boldsymbol{A}^{WI}$, $\boldsymbol{A}^{IW}$, $\boldsymbol{A}^{II}$, and $\boldsymbol{B}^{WW}$, $\boldsymbol{B}^{WI}$, $\boldsymbol{B}^{IW}$, $\boldsymbol{B}^{II}$, is, respectively, $2N_w\times 2N_w$, $2N_w\times 2N_s$, $2N_s\times 2N_w$, $2N_s\times 2N_s$. Collecting (4.23) and (4.24), we obtain the block linear system

$$\left[\begin{array}{c|c} \boldsymbol{A}^{WW} & -(1-\lambda)\,\boldsymbol{B}^{WI} \\ \hline \boldsymbol{A}^{IW} & -(1-\lambda)\left(\boldsymbol{B}^{II}-\tfrac{1}{2}\,\boldsymbol{I}\right)+\lambda\,\boldsymbol{I} \end{array}\right]\cdot\left[\begin{array}{c} \boldsymbol{f}^{DW} \\ \boldsymbol{u}^{D1I} \end{array}\right] = \left[\begin{array}{c|c|c} \boldsymbol{B}^{WW}-\tfrac{1}{2}\,\boldsymbol{I} & -\boldsymbol{A}^{WI} & -\lambda\,\boldsymbol{B}^{WI} \\ \hline \boldsymbol{B}^{IW} & -\boldsymbol{A}^{II} & -\lambda\left(\boldsymbol{B}^{II}-\tfrac{1}{2}\,\boldsymbol{I}\right)-\lambda\,\boldsymbol{I} \end{array}\right]\cdot\left[\begin{array}{c} \boldsymbol{u}^{DW} \\ \Delta\boldsymbol{f}^{DI} \\ \Delta\boldsymbol{u}^{RI} \end{array}\right] \quad (4.25)$$

The size of the square matrix on the left-hand side is $2(N_w+N_s)\times 2(N_w+N_s)$, and the size of the rectangular matrix on the right-hand side is $2(N_w+N_s)\times 2(N_w+2N_s)$. The solution is found by the method of Gauss elimination. Note that the wall–wall (WW) matrices are independent of the location of the interface and need to be computed only once, at the beginning of the simulation.

In the present implementation, the interfacial elements are straight segments defined by convected endpoints, and the wall elements are either straight segments or circular arcs defined by fixed endpoints. The unit normal vector and curvature over the interface are computed by cubic-spline interpolation in terms of the instantaneous position of the surface nodes. To ensure the accuracy and longevity of the simulation, the interfacial nodes are dynamically redistributed according to criteria on the maximum and minimum separation and local curvature. Other computational procedures, including a method for integrating in time the convection–diffusion equation for the surfactant concentration, are discussed by Blyth & Pozrikidis (2004*a*).

4.3. *Results and discussion*

In the numerical simulations, we consider shear-driven flow in a horizontal channel with neutrally buoyant fluids. Figure 10(*a*) shows steady interfacial profiles for flow in a channel confined by a lower sinusoidal wall with amplitude $a_w/L=0.01$, 0.10 and

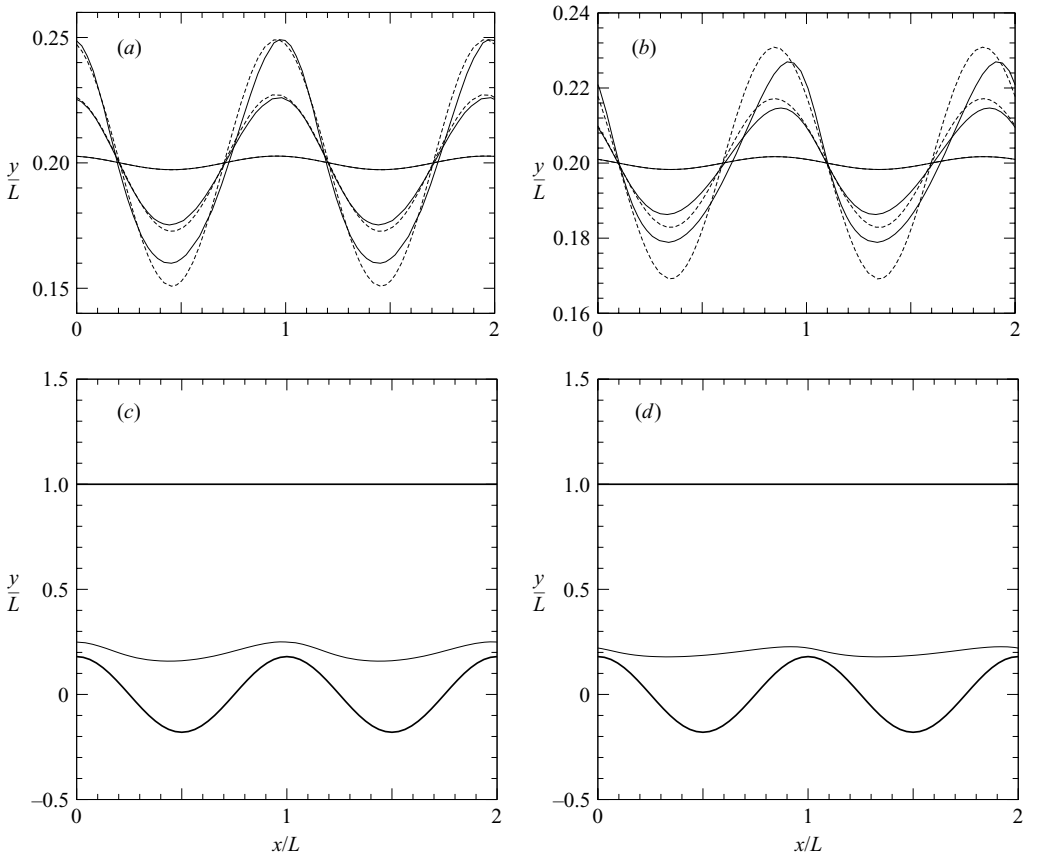

FIGURE 10. Steady interfacial profiles for shear-driven flow over a sinusoidal wall with $h_1/L = 0.20$, $d/L = 1.0$, $Ca = 2$, $Ma = 0$ and wall amplitude $a_w/L = 0.01$, 0.10 and 0.18, with (*a*) $\lambda = 1$, and (*b*) $\lambda = 0.2$. The dashed lines represent the predictions of the linear perturbation theory for small-amplitude corrugations. Wall and free-surface profiles for $a_w/L = 0.18$ are shown in (*c*) for $\lambda = 1$ and (*d*) 0.2, on a physical scale.

0.18, for $h_1/L = 0.20$, $d/L = 1.0$, $Ca = 2$, $\lambda = 1$, in the absence of a surfactant, $Ma = 0$. The lower film thickness is defined as $h_1 = A/L$, where A is the film area within each period. The solid lines in figure 10(*a*) represent the numerical results produced by the boundary-element method, and the broken lines represent the predictions of the linear perturbation analysis. The numerical and analytical results are virtually indistinguishable for the small amplitude, and in good agreement for the moderate amplitude. Significant deviations are observed near the troughs for the large amplitude. In all cases, the linear perturbation analysis somewhat overestimates the deformation of the interface. Figure 10(*c*) illustrates wall and interfacial profiles for $a_w/L = 0.18$ on a physical scale. Figure 10(*b*) shows corresponding results for the same conditions except that $\lambda = 0.2$, where the lower fluid viscosity is five times the upper fluid viscosity. Physically, a low-viscosity cleaning liquid is sheared over a viscous fluid coated on the wavy wall. In this case, the perturbation analysis is accurate for the small wave amplitude, but overestimates the deformation of the interface by a sizeable amount for the large amplitude even though the deformation of the interface is less pronounced than that for $\lambda = 1$. Figure 10(*d*) illustrates the wall and interfacial profiles for $a_w/L = 0.18$ on a physical scale.

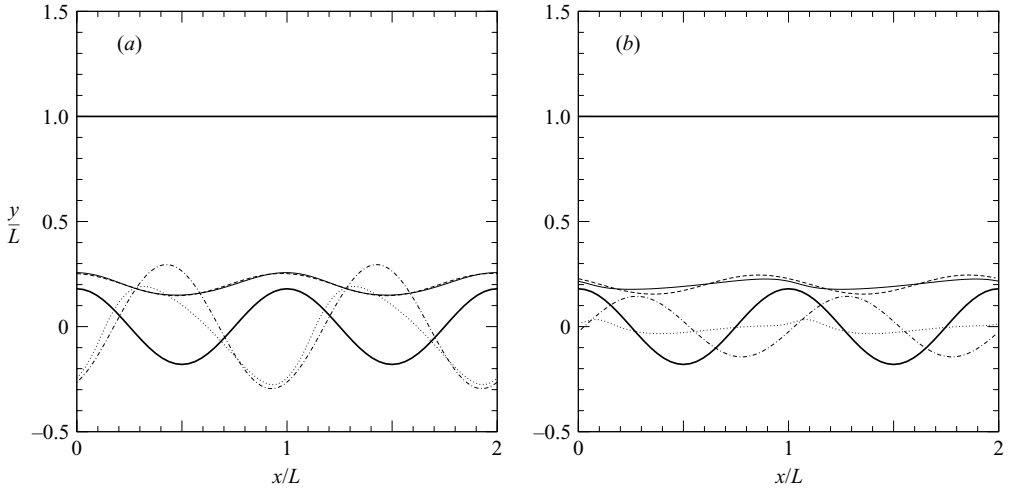

FIGURE 11. Interfacial profiles (solid and dashed lines), and distribution of the surfactant concentration (dotted and dashed-dotted lines) for shear-driven flow over a sinusoidal wall with $h_1/L = 0.20$, $d/L = 1.0$, $Ca = 2$, $a_w/L = 0.18$, $Ma = 1$ and (*a*) $\lambda = 1$, (*b*) 0.20.

Next, we consider flow in the presence of a non-diffusing surfactant. Figure 11 shows steady interfacial profiles for flow over a sinusoidal wall with $h_1/L = 0.20$, $d/L = 1.0$, $Ca = 2.0$, $a_w/L = 0.18$, $Ma = 1$ and $\lambda = 1$ or 0.2. The solid lines represent numerical results obtained with the boundary-element method, and the dashed lines represent the predictions of the linear perturbation analysis. The dotted lines show the distribution of the reduced and normalized surfactant concentration, $(\Gamma - \bar{\Gamma})/\bar{\Gamma}$, where $\bar{\Gamma}$ is the x-averaged value over one period, and the dot-dashed lines show the corresponding predictions of the linear perturbation theory. For $\lambda = 1$, the linear perturbation analysis somewhat overestimates the non-uniformity in the surfactant concentration near the peaks above the troughs of the sinusoidal wall. Because there is a surplus of surfactant at the troughs and a deficit at the peaks, the surface tension is low at the troughs and high at the peaks, and the associated Marangoni traction drives a flow away from the valleys. Since the surfactant diffusivity is zero, the surfactant transport equation at steady state simplifies to $\partial(u_t\Gamma)/\partial l = 0$, which means that the product $u_t\Gamma$ is constant along the interface. Correspondingly, the tangential velocity is low at the troughs and high at the peaks, in agreement with physical intuition. For $\lambda = 0.2$, the theory predicts a significant non-uniformity, whereas the boundary integral solution reveals a nearly uniform distribution over the wavy interface.

Figure 12 shows steady interfacial profiles for flow over a planar wall containing a periodic sequence of semi-circular cavities or protrusions, for the conditions described in the caption. In both cases, the film thickness is defined as $h_1 = A/L$, where A is the film area above the flat portion of the wall between the projections or depressions. In the case of flow over cavities, as the film thickness becomes smaller, the interface penetrates the cavity openings and reaches a minimum thickness at the rim. In the case of flow over protrusions, a minimum film thickness exists under which steady solutions with a contiguous interface cannot be found. In reality, the interface breaks up into sections attached to the protrusions at positions determined by the contact angle. The numerical results indicate that, for the particular geometry considered, breakup will occur when the film thickness is just under $h_1/L = 0.175$.

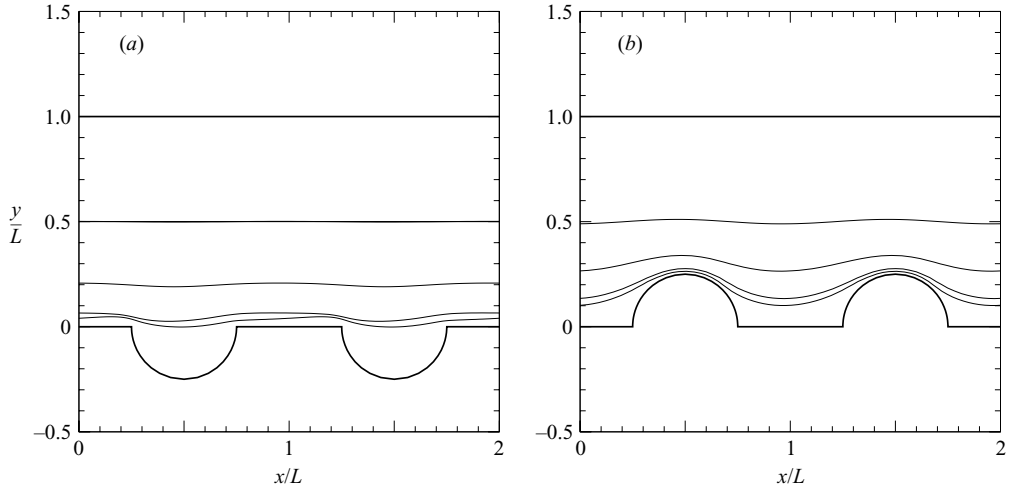

FIGURE 12. Steady interfacial profiles for shear-driven flow over a planar wall with (*a*) a periodic sequence of semi-circular cavities and film thicknesses $h_1/L = 0.025$, 0.05, 0.20 and 0.50, and (*b*) a periodic sequence of semi-circular protrusions and film thicknesses $h_1/L = 0.175$, 0.20, 0.30 and 0.50. In both cases, $d/L = 1.0$, $Ca = 2$, $Ma = 0$ and $\lambda = 1$.

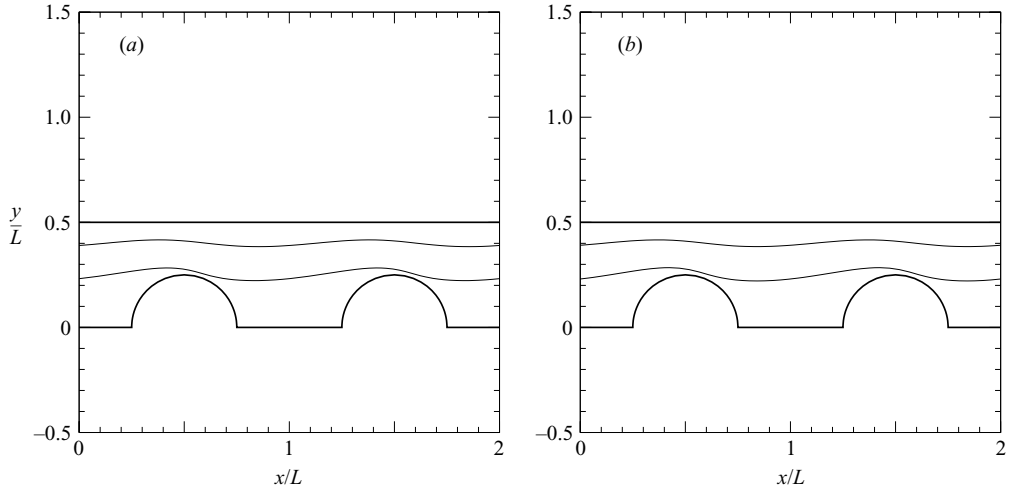

FIGURE 13. Steady interfacial profiles for pressure-driven flow over a planar wall containing a sequence of semi-circular protrusions for $d/L = 0.5$, $\gamma_0/(\chi L^2) = 0.5$, $Ma = 0$, $h_1/L = 0.25$ and 0.40 and (*a*) $\lambda = 1$ or (*b*) 0.20.

Qualitatively similar results were obtained for difference wall geometries and flow conditions. For example, figure 13 shows steady interfacial profiles for pressure-driven flow in a narrow channel, $U = 0$ and $\chi \neq 0$, for $d/L = 0.5$, $\gamma_0/(\chi L^2) = 0.5$, $Ma = 0$ and $\lambda = 1$ or 0.20. The lower wall contains a sequence of semi-circular protrusions of radius $R/L = 0.25$. Comparing the frames presented in this figure, we find that the viscosity ratio has a negligible effect on the deformation of the interface.

5. Conclusion

We have studied the structure of two-layer flow in a channel with a planar upper wall and an uneven lower wall in the limit of vanishing Reynolds number. The interface

may be clean or occupied by an insoluble surfactant. First, a linear perturbation analysis was performed for small-amplitude sinusoidal corrugations, and graphs of the interface amplitude and phase shift were presented to illustrate the effect of the wavenumber, capillary number, viscosity ratio, film thickness and Marangoni number. The analysis revealed that, as in the case of film flow down an inclined wall (Pozrikidis 2003), the surfactant generally amplifies the deformation of the interface and causes a negative drift in the phase shift. The effect of the surfactant is most significant for corrugations whose wavelength is large compared to the adjacent layer thickness, intermediate capillary numbers, and when the film coated on the wavy wall is more viscous than the upper fluid. As the interface approaches the upper planar wall, the interfacial profile tends to become in phase with the lower corrugated wall in the presence or absence of surfactant, revealing the wall topography. In the second part of this paper, we developed a boundary-integral formulation for simulating the evolution of the interface from a specified initial condition, and presented numerical simulations to establish the range of validity of the linear theory. Further results of the boundary-integral simulations illustrated the structure of the flow over a planar wall with indented topography.

In the absence of surfactant, the two-layer unidirectional channel flow is stable in the limit of vanishing Reynolds number. Introducing surfactant may initiate a new type of instability attributed to the Marangoni traction (e.g. Blyth & Pozrikidis 2004*a*; Pozrikidis 2004). Though wall corrugations whose wavenumber falls in the unstable regime are likely to promote this instability, the precise effect can only be assessed by carrying out a formal stability analysis similar to that presented by Kouris & Tsamopoulos (2000, 2001) and Wei & Rumschitzki (2002*a*, *b*) for long waves in core–annular flow, as discussed in § 1. Unfortunately, the dual perturbation expansion with respect to the wall and flow perturbation amplitudes requires a further assumption regarding their relative magnitude, or else leads to a mathematical problem of formidable complexity. In recent work, we have described the structure of the steady flow at non-infinitesimal Reynolds numbers by perturbation expansions for small wall amplitudes, and numerical methods based on the immersed boundary formulation in curvilinear coordinates for arbitrary wall amplitudes. (Luo, Blyth & Pozrikidis 2005).

This work was supported by a grant provided by the National Science Foundation.

REFERENCES

Adamson, A. W. 1990 *Physical Chemistry of Surfaces*. Wiley.

Blyth, M. G. & Pozrikidis, C. 2004*a* Effect of surfactants on the stability of two-layer channel flow. *J. Fluid Mech.* **505**, 59–86.

Blyth, M. G. & Pozrikidis, C. 2004*b* Effect of surfactant on the stability of film flow down an inclined plane. *J. Fluid Mech.* **521**, 241–250.

Dassori, C. G., Deiber, J. A. & Cassano, A. E. 1984 Slow two-phase flow through a sinusoidal channel. *Intl J. Multiphase Flow* **10**, 181–193.

Kalliadasis, S., Bielarz, C. & Homsy, G. M. 2000 Steady free-surface thin film flows over topography. *Phys. Fluids* **12**, 1889–1898; addendum in **12**, 3305.

Kouris, C. & Tsamopoulos, J. 2000 Concentric core–annular flow in a circular tube of slowly varying cross-section. *Chem. Engng Sci.* **55**, 5509–5530.

Kouris, C. & Tsamopoulos, J. 2001 Concentric core–annular flow in a periodically constricted circular tube. Part 1. Steady-state, linear stability and energy analysis. *J. Fluid Mech.* **432**, 31–68.

Li, X. & Pozrikidis, C. 1997 The effect of surfactants on drop deformation and on the rheology of dilute emulsions in Stokes flow. *J. Fluid Mech.* **341**, 165–194.

Luo, H., Blyth, M. G. & Pozrikidis, C. 2005 Two-layer flow in a corrugated channel. *J. Engng Maths.* Submitted.

Mazouchi, A. & Homsy, G. M. 2001 Free surface Stokes flow over topography. *Phys. Fluids* **13**, 2751–2761.

Pozrikidis, C. 1992 *Boundary Integral and Singularity Methods for Linearized Viscous Flow*. Cambridge University Press.

Pozrikidis, C. 2001 Interfacial dynamics for Stokes flow. *J. Comput. Phys.* **169**, 250–301.

Pozrikidis, C. 2002 *A Practical Guide to Boundary Element Methods with the Software Library BEMLIB*. Chapman & Hall/CRC Press.

Pozrikidis, C. 2003 Effect of surfactants on film flow down a periodic wall. *J. Fluid Mech.* **496**, 105–127.

Pozrikidis, C. 2004 Instability of multi-layer channel and film flows. *Adv. Appl. Mech.* **40**, 179–239.

Wei, H.-H. & Rumschitzki, D. S. 2002*a* The linear stability of a core–annular flow in an asymptotically corrugated tube. *J. Fluid Mech.* **466**, 113–147.

Wei, H.-H. & Rumschitzki, D. S. 2002*b* The weakly nonlinear interfacial stability of a core–annular flow in a corrugated tube. *J. Fluid Mech.* **466**, 149–177.